JOURNAL OF GEOPHYSICAL RESEARCH, VOL. 113, B08319, doi:10.1029/2007JB005182, 2008

Attenuation of radiated ground motion and stresses from three-dimensional supershear ruptures

Eric M. Dunham[1] and Harsha S. Bhat[2]

Received 23 May 2007; revised 14 April 2008; accepted 20 May 2008; published 30 August 2008.

[1] Radiating shear and Rayleigh waves from supershear ruptures form Mach waves that transmit large-amplitude ground motion and stresses to locations far from the fault. We simulate bilateral ruptures on a finite-width vertical strike-slip fault (of width W and half-length L with $L \gg W$) breaking the surface of an elastic half-space, and focus on the wavefield out to distances comparable to L. At distances much smaller than W, two-dimensional plane-strain slip-pulse models (i.e., models in which the lateral extent of the slip zone is unbounded) accurately predict the subsurface wavefield. Amplitudes in the shear Mach wedge of those models are undiminished with distance from the fault. When viewed from distances far greater than W, rupture is accurately modeled as a moving point source that produces a shear Mach cone and, on the free surface, Rayleigh-wave Mach fronts. Geometrical spreading of the shear Mach cone occurs radially and amplitudes there decrease with the inverse square-root of distance. The transition between these two asymptotic limits occurs at distances comparable to W. Similar considerations suggest that Rayleigh Mach waves suffer no attenuation in the ideally elastic medium studied here. The rate at which fault strength weakens at the rupture front exerts a strong influence on the off-fault fields only in the immediate vicinity of the fault (for both sub-Rayleigh and supershear ruptures) and at the Mach fronts of supershear ruptures. More rapid weakening generates larger amplitudes at the Mach fronts.

Citation: Dunham, E. M., and H. S. Bhat (2008), Attenuation of radiated ground motion and stresses from three-dimensional supershear ruptures, *J. Geophys. Res.*, *113*, B08319, doi:10.1029/2007JB005182.

1. Introduction

[2] The velocity at which a rupture propagates influences the amplitude and character of the radiated ground motion and stresses. A distinct manifestation of this occurs when ruptures exceed the S-wave speed and generate shear Mach waves that efficiently transmit ground motion and stresses away from the fault. Supershear speeds are also super-Rayleigh ones, and in an elastic half-space, we also expect Rayleigh Mach waves propagating along the free surface. Slip alters the component of normal stress parallel to the rupture front; for vertical strike-slip faults, negation of these stresses on the free surface generates Rayleigh waves. It follows from this line of reasoning that Rayleigh Mach fronts will be generated even if the rupture propagates at $\sqrt{2}$ times the S-wave speed, the unique speed at which no shear Mach waves are produced [*Eshelby*, 1949]. The Rayleigh Mach front originates near the intersection of the rupture front with the free surface, and as one moves away from the fault along the free surface, the Rayleigh Mach front lags behind the shear Mach front. The expected pattern of shear and Rayleigh Mach fronts is illustrated in Figure 1.

[3] The objective of the current work is to quantify how the amplitude of radiated waves, specifically of those associated with the Mach waves, diminishes with distance from the fault. We further compare fields from supershear ruptures to those produced by sub-Rayleigh ruptures with the aim of contrasting the rate at which amplitudes decay with distance from the fault for both classes of ruptures.

[4] Supershear propagation, first suggested by analytical [*Burridge*, 1973] and numerical [*Andrews*, 1976; *Das and Aki*, 1977] studies, has since been confirmed in laboratory experiments [*Rosakis et al.*, 1999; *Xia et al.*, 2004]. Supershear speeds have been reported for a number of earthquakes, primarily from analyses of near-source records of the 1979 Imperial Valley [*Archuleta*, 1984; *Spudich and Cranswick*, 1984], 1999 Izmit and Düzce [*Bouchon et al.*, 2001, 2002], and 2002 Denali fault [*Ellsworth et al.*, 2004; *Dunham and Archuleta*, 2004] events. As *Savage* [1971] and *Ben-Menahem and Singh* [1981] have shown, there are also distinctive features of supershear ruptures at regional and teleseismic distances (e.g., changes in the radiation pattern), and an inversion of the 2001 Kokoxili (Kunlun) event [*Bouchon and Vallée*, 2003] using regional Love waves suggests supershear propagation. This conclusion is also supported by inversions of teleseismic body waves

[1]Department of Earth and Planetary Sciences and School of Engineering and Applied Sciences, Harvard University, Cambridge, Massachusetts, USA.
[2]Department of Earth Sciences, University of Southern California, Los Angeles, California, USA.

0148-0227/08/2007JB005182$09.00

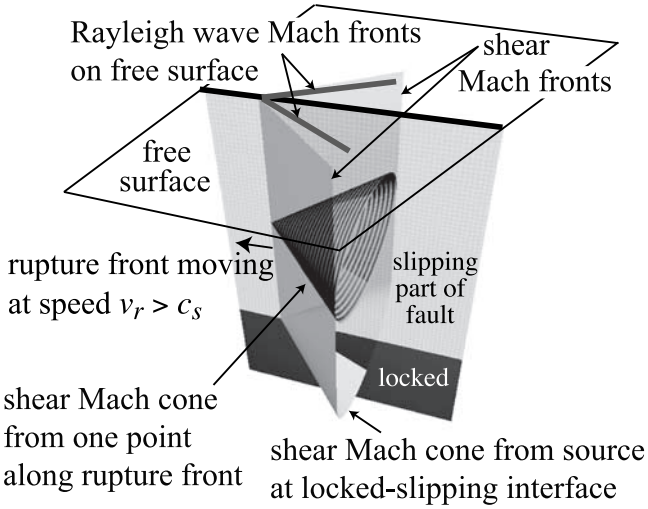

Figure 1. Shear and Rayleigh Mach fronts emitted by a supershear rupture on a surface-breaking strike-slip fault of finite width. Each point on the rupture front acts as a source and produces a shear Mach cone. The superposition of the Mach cones generated by each point along the rupture front manifests as a shear Mach wedge (a planar wavefront), capped at the bottom edge of the fault by half of a cone. Rayleigh Mach fronts on the free surface emanate from the intersection of the rupture front with the free surface.

[*Robinson et al.*, 2006], though not all studies of such waves reach such a strong conclusion [*Antolik et al.*, 2004]. The unique characteristics of near-source records from supershear events, particularly of records at Pump Station 10 (located only 3 km from fault) in the 2002 Denali fault event, prompted a closer look at characteristics of radiated ground motion from supershear ruptures.

[5] We build on a number of previous studies that have examined the influence of rupture speed on near-source ground motion. *Ben-Menahem and Singh* [1987] studied the acceleration field generated by a point velocity dislocation (a singularity moving along a line and leaving in its wake a fixed moment per unit length) that travels a finite distance at a supershear speed before stopping. In addition to starting and stopping phases, shear Mach waves were implicated as carriers of large-amplitude accelerations. Their results further demonstrate how the Mach wave only passes through a particular region surrounding the fault. By considering propagation only along a line, their analysis applies only to observation points sufficiently removed from the fault (i.e., at distances much greater than the fault width). A number of other researchers have focused on the wavefield in the immediate vicinity of the fault (extending out to distances comparable to the fault width, but not much beyond that). By examining a sequence of kinematic models with various rupture speeds, *Aagaard and Heaton* [2004] demonstrated how the well-known two-sided fault-normal velocity waveform of sub-Rayleigh ruptures (the so-called "directivity pulse" that has been of primary concern in seismic hazard [*Somerville et al.*, 1997]) vanishes when ruptures exceed the S-wave speed. Instead, the largest amplitudes now occur at the Mach front. *Bernard and Baumont* [2005] combined kinematic models of supershear ruptures with an asymptotic isochrone-based analysis of fields near the Mach front to explore features of the Mach wave from supershear ruptures. Their asymptotic analysis, which did not include any corrections for a finite fault width, showed that for straight ruptures fronts, field amplitudes at the Mach front remain undiminished with distance from the fault; rupture-front curvature leads to an inverse square-root decay of amplitudes with distance due to a loss of coherence at the Mach front.

[6] The starting point for our analysis is the two-dimensional (2D) steady state slip-pulse model developed by *Rice et al.* [2005] to examine stress fields near the rupture front of sub-Rayleigh ruptures. This model was extended to supershear speeds by *Dunham and Archuleta* [2005] and *Bhat et al.* [2007]. *Dunham and Archuleta* [2005] focused on ground motion (specifically, velocity records) from slip pulses in the context of models of the Denali fault event [*Ellsworth et al.*, 2004; *Dunham and Archuleta*, 2004]. *Bhat et al.* [2007] studied the off-fault damage pattern due to supershear ruptures and hypothesized that anomalous ground cracking observed at a few tens of kilometers from the fault during the 2001 Kokoxili (Kunlun) event resulted from the high stresses at the Mach front emanating from a supershear rupture. This observation raises the possibility that radiated stresses from a large supershear event might trigger slip on adjacent faults of the proper orientation. One objective of the current work is to quantify how the amplitude of Coulomb stresses on pre-existing structures is influenced by rupture speed and the finite fault width, and whether or not these amplitudes are sufficient to activate secondary faulting.

[7] The most distinctive feature of the 2D supershear slip-pulse models is the shear Mach wave. The combined assumptions of two dimensions (i.e., an infinite extent of the slipping region parallel to the rupture front), steady state propagation, and a homogeneous linear elastic medium cause the Mach waves to extend infinitely far from the fault and for the amplitude of fields at the Mach fronts to remain undiminished with distance from the fault. This study addresses the first of these assumptions by considering ruptures in three dimensions (3D), specifically right-lateral strike-slip ruptures on a finite-width vertical fault breaking the surface of an elastic half-space. The focus is on the wavefield after the rupture has propagated many times further than the fault width. In addition to the shear Mach waves found in 2D models, we also expect Rayleigh Mach waves emanating from the rupture front out along the free surface. The 2D plane-strain models feature large changes in the normal stress parallel to the rupture front. These changes appear only in the vicinity of the fault and not further away at the shear Mach front since fields there are nondilatational. When considering rupture in a half-space, the component of normal stress parallel to the rupture front is also normal to the free surface and must be negated there to satisfy the traction-free boundary condition. This can be accomplished by the superposition of normal loads on the free surface that negate the moving vertical-normal-stress pattern. These moving loads, which propagate at a super-Rayleigh speed, will then excite Rayleigh Mach waves [*Lansing*, 1966; *Georgiadis and Lykotrafitis*, 2001]. Since these waves are being excited by dilatational stresses,

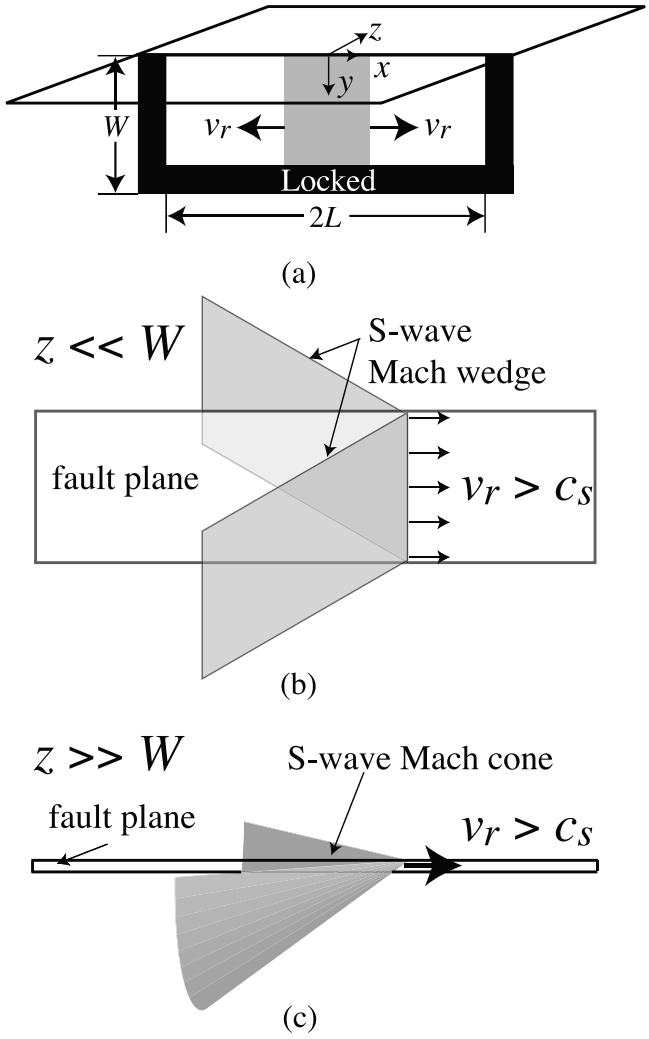

Figure 2. (a) Rupture on a fault of width W and half-length L that expands bilaterally at speed v_r. (b) Shear Mach wedge from a steady state supershear rupture in 2D, which approximates S-wave radiation from slip on a finite-width fault at locations close to the fault ($z \ll W$) and away from the fault edges. (c) Shear Mach cone emitted by supershear line source, which approximates S-wave radiation from slip on a finite-width fault when viewed from afar ($z \gg W$).

Rayleigh Mach waves will exist even at $\sqrt{2}$ times the S-wave speed.

[8] To understand the effect of bounding the vertical extent of the slipping region, consider two limiting cases of rupture on a vertical surface-breaking fault of width W and half-length L (Figure 2a). At locations close to the fault and away from its edges and the free surface (specifically, at locations much closer that W), the fault width is unimportant and 2D models provide an accurate description of the fields, at least if the length of the slip-weakening zone, R, is much less than W. In this extremely near-source region, the shear Mach front assumes the form of a wedge (Figure 2b) and Mach-wave amplitudes will not diminish with distance from the fault. Of course, this region is further complicated by the presence of dilatational fields of comparable amplitude. At the opposite extreme, consider points far removed from the fault (specifically, at distances greatly exceeding W). From these distant points, the fault appears as a line source, and S-wave radiation now forms a Mach cone (Figure 2c). Since the cross-section of the cone is a circle, geometrical spreading dictates that Mach-wave amplitudes will decrease with the inverse square-root of radial distance from the fault. (Also, it is not clear that the Rayleigh Mach-wave amplitudes would attenuate at all, in the ideally elastic material considered.) It is of critical importance to hazard calculations to understand exactly how the transition between these two extremes occurs. Specifically, to what distances are large ground motion and stresses transported for realistic fault geometries? *Bhat et al.* [2007] hypothesized that the transition between the two limits occurs at distances comparable to W, and our results confirm this hypothesis, although the Rayleigh Mach fronts also contribute to the fields.

2. Model Geometry

[9] We model ruptures on a vertical right-lateral strike-slip fault that intersects the free surface (Figure 2a). W is the fault width, and v_r is the rupture velocity; we study three representative values of v_r: 0.8 c_s, 1.3 c_s, and 1.6 c_s, where c_s is the S-wave speed. The sub-Rayleigh speed, 0.8 c_s, was chosen as mid-range of the typical speed range (0.7-0.9 c_s) inferred for most earthquakes. Two speeds are necessary within the intersonic range, since the sign of the radiated shear fields changes as the Eshelby speed, $\sqrt{2}\ c_s$, (at which no S-waves are generated) [*Eshelby*, 1949] is crossed. Stability considerations [*Burridge et al.*, 1979; *Obrezanova and Willis*, 2003] suggest ruptures should only propagate above a speed close to $\sqrt{2}\ c_s$, and most of the previously mentioned inversions have found speeds in this range. Consequently we focus primarily on $v_r = 1.6\ c_s$ within the supershear regime, but also present results for $v_r = 1.3\ c_s$, which lies on the opposite side of the Eshelby speed. We also study rupture at exactly $\sqrt{2}\ c_s$ to confirm that Rayleigh Mach waves exist at this speed, but do not otherwise focus on this case. For simplicity, we keep v_r fixed (rather than considering a more natural transition from sub-Rayleigh to supershear speeds, which would generate a more complicated set of waveforms) and consider symmetrically expanding bilateral ruptures that propagate a distance L in each direction. We also wish to work in the context of a dynamic model, in the sense that we specify a constant stress drop, $\Delta\sigma$, within the rupture. In this sense, our models are closely related to self-similar singular crack models in 2D. In our work, we prevent a stress singularity at the rupture front by employing a cohesive zone model that can be interpreted in the context of the commonly used slip-weakening friction law. The parameters of this model are the peak and residual strengths, τ_p and τ_r, and the distance, R, over which strength drops from τ_p to τ_r. As discussed by *Dunham and Archuleta* [2005] and *Bhat et al.* [2007], the extent of the slip-weakening zone (relative to the length of the rupture) plays a large role in determining the maximum amplitude of fields at the Mach front.

[10] The specific procedure we use to force ruptures with the desired properties was originally employed by *Andrews* [1985]. The shear strength of the fault, τ_{str}, weakens linearly

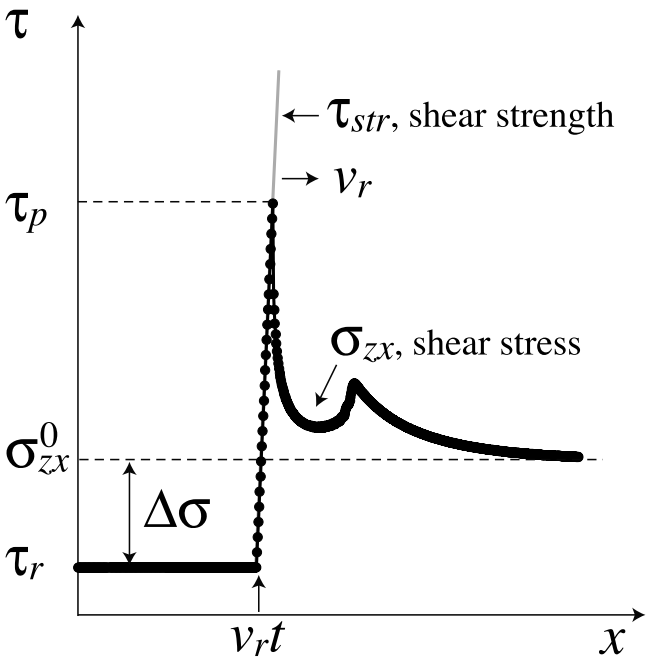

Figure 3. Fracture criterion used to force a rupture at speed v_r with stress drop $\Delta\sigma$. Fault strength increases linearly from $|x| = v_r t$ (gray line). When shear stress on the fault (black line and points from our numerical model at $v_r = 0.8\ c_s$) reaches the strength, slip commences.

with distance (with weakening rate A) behind the rupture front:

$$\tau_{str}(x,t) = \max\{\tau_r, \tau_r + A(|x| - v_r t)\}. \quad (1)$$

The fault is locked until stress reaches the fault strength, τ_p (which is not specified a priori in this approach, but depends on τ_r and A, and varies moderately with the position of the rupture tip), at which time slip commences and weakening occurs in such a way as to ensure that stress always equals strength during sliding. This is illustrated in Figure 3. In this model, both τ_p and R evolve as the rupture expands in order to provide a solution with nonsingular and continuous stress at the tip. An associated energy release rate, or fracture energy G, can then be inferred as the area under the resulting plot of $\tau - \tau_r$ versus slip. In 2D self-similar crack models, the energy release rate increases linearly with propagation distance; the procedure we use, if applied in this context, results in an increase of both τ_p and R to accommodate the increasing energy flux into the slip-weakening zone.

[11] We note several other important quantities that will be of interest to us. The first is the seismic S ratio $[S = (\tau_p - \sigma^0_{zx})/(\sigma^0_{zx} - \tau_r)]$, a measure of the initial load, σ^0_{zx}, relative to the peak and residual strengths. The stress drop is $\Delta\sigma = \sigma^0_{zx} - \tau_r$ and the strength drop is $\tau_p - \tau_r$. The fracture energy, G, may be calculated for each point on the fault as

$$G = \int [\tau(t) - \tau_r] V(t) dt = \int [\tau(\delta) - \tau_r] d\delta, \quad (2)$$

Table 1. Representative Dimensionalizing Factors by Which Nondimensional Values Reported in This Study May Be Converted to Physical Values; a Range Exists Due to Uncertainty in $\Delta\sigma$[a]

Field, scale (units)	Low Stress Drop	Moderate Stress Drop	Large Stress Drop
Stress, $\Delta\sigma$ (MPa)	0.3	3	30
Velocity, $\Delta\sigma c_s/\mu$ (m/s)	0.03	0.3	3
Displacement, $\Delta\sigma W/\mu$ (m)	0.1	1	10
Fracture energy, $\Delta\sigma^2 W/\mu$ (MJ/m^2)	0.03	3	300

[a]Other parameters employed in these relations are $\mu = 30$ GPa, $c_s = 3$ km/s, and $W = 10$ km.

in which V is the slip velocity and the integrals are taken over all time t or all slip δ. Finally, we define an equivalent slip-weakening distance D_c via the relation

$$G = \frac{1}{2}(\tau_p - \tau_r) D_c, \quad (3)$$

which proves useful when interpreting our results in the context of the commonly used linear slip-weakening law [*Andrews*, 1976].

[12] We next nondimensionalize the model by scaling all distances by W and time by W/c_s. Stress is scaled with $\Delta\sigma$, particle and slip velocities by $\Delta\sigma c_s/\mu$ where μ is the shear modulus. Displacements and slip scale with $\Delta\sigma W/\mu$. When considering physical values of these parameters, we take $\mu =$ 30 GPa, $c_s = 3$ km/s and $W = 10$ km. We consider a Poisson material (i.e., one for which the P-wave speed is given by $c_p = \sqrt{3}\ c_s$), and choose τ_r to yield a dynamic coefficient of friction of 0.2 (but note that the actual value of normal stress, σ^0_{zz}, is unimportant since normal stress on the fault remains unaltered by slip on vertical strike-slip faults in a homogeneous medium). Estimates of stress drop vary widely, and to encompass this range, we consider three representative values of $\Delta\sigma$: 0.3 MPa, 3 MPa, and 30 MPa. We report nondimensional values (denoted by a superscript *) in our figures, and these may be easily converted to physical values by the scaling factors described above and summarized for reference in Table 1.

[13] We numerically solve our problem with a staggered-grid finite-difference code [*Favreau et al.*, 2002] with fault boundary conditions implemented with the staggered-grid split-node (SGSN) method of *Dalguer and Day* [2007]. Rake rotation is permitted, in that the slip vector rotates so as to be aligned with the shear traction

Table 2. Model Parameters, Reported as Both Nondimensional Values and When Dimensionalized in the Case That $\Delta\sigma = 3$ MPa for $v_r = 0.8\ c_s$ (See Table 1 and Text for Further Discussion of the Dimensionalization Method)[a]

v_r/c_s	S	A*	G*	D_c*	$\Delta\sigma$ (MPa)	A (MPa/km)	R (km)
0.8	2.03	7.00	3.19	2.10	3.00	2.10	4.33
1.3	1.28	2.71	1.80	1.58	3.99	1.08	8.42
1.6	0.53	3.72	0.82	1.06	5.92	1.93	4.71

[a]Note that G, $\tau_p - \tau_r$, D_c, and S increase with propagation distance in our model; the values reported here are measured at $x = 8\ W$ in the 2D geometry. Parameters which are independent of v_r are $G = 9.57$ MJ/m^2, $\tau_p - \tau_r = 9.09$ MPa, and $D_c = 2.10$ m.

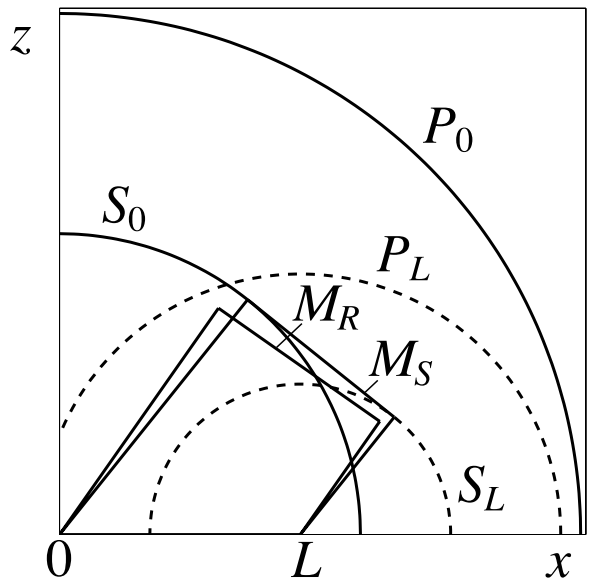

Figure 4. Wavefronts from an expanding supershear rupture that stops after propagating a distance L. The starting phases are marked as P_0 and S_0, the stopping phases as P_L and S_L, and the Rayleigh and shear Mach fronts as M_R and M_s. Only points within the trapezoidal regions have experienced the passage of the respective Mach waves. A number of other wavefronts, such as head waves, Rayleigh waves on the fault, and Rayleigh-wave diffractions, are not shown.

vector. The degree of rake rotation depends on the change in stress relative to the initial level of stress in the medium. In our simulations, $\sigma^0_{zx}/(\sigma^0_{zx} - \tau_r) = 1.2$ and we have no transverse shear load (i.e., $\sigma^0_{zy} = 0$). The method is fourth order in space and second order in time for wave propagation in the body, but the spatial order is reduced to second order at the fault. We implement the free-surface boundary condition using the fourth-order W-AFDA scheme proposed by *Kristek et al.* [2002] (which collocates the free surface with the grid points for vertical velocity and normal stresses), and place perfectly matching layer (PML) absorbing boundaries on the remaining sides [*Marcinkovich and Olsen*, 2003]. Ruptures propagate for 15 W in each direction before reaching the end of the fault (we lock the fault beyond this), but the computational domain extends in this direction out to ±20 W to permit an examination of stopping phases. The fault-normal extent of the computational domain is 15 W. We run each simulation for a duration that permits the S-wave stopping phase from the fault ends to reach 15 W in the fault-normal direction for any x. We discretize the medium with a uniform grid spacing of $h^* = 0.02$ (i.e., a grid spacing of $h = 200$ m for $W = 10$ km, which is far larger than desired if the estimates of slip-weakening zone sizes R of a few tens of meters at mid-seismogenic depths *Rice et al.* [2005] are accurate). Numerical resolution is discussed below, but we note here that the resolution is determined by the choice of the cohesive-zone parameter A^*; larger A implies smaller R.

[14] The 2D case provides a convenient starting point to calibrate the numerical method, and it further provides

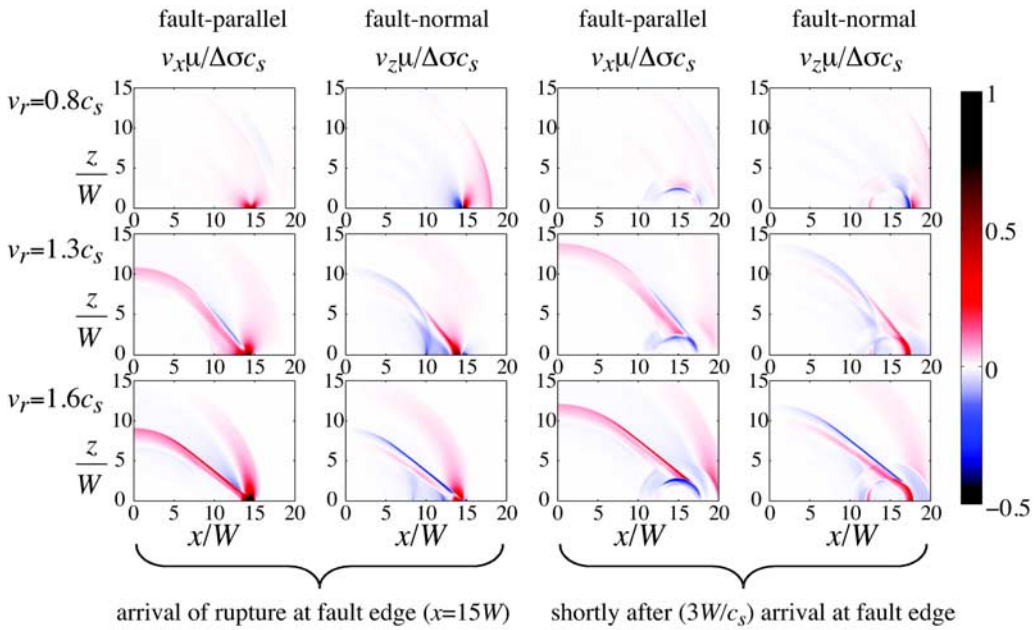

Figure 5. Snapshots of the free-surface velocity field for various ruptures speeds at two times: just as the rupture arrives the edge of the fault and at a slightly later time (an additional 3 W/c_s after the arrival) to emphasize the stopping phases. Ruptures have identical G, $\tau_p - \tau_r$, and D_c but different $\Delta\sigma$. Note that the value of $\Delta\sigma$ used to nondimensionalize the velocities is different for each rupture speed (see Table 1). The color scale is saturated for positive values to emphasize field amplitudes away from the rupture front. The closely coincident shear and Rayleigh Mach fronts can most clearly be seen in the fault-normal component for $v_r = 1.6\ c_s$ since the sign of this component is opposite for the two fronts.

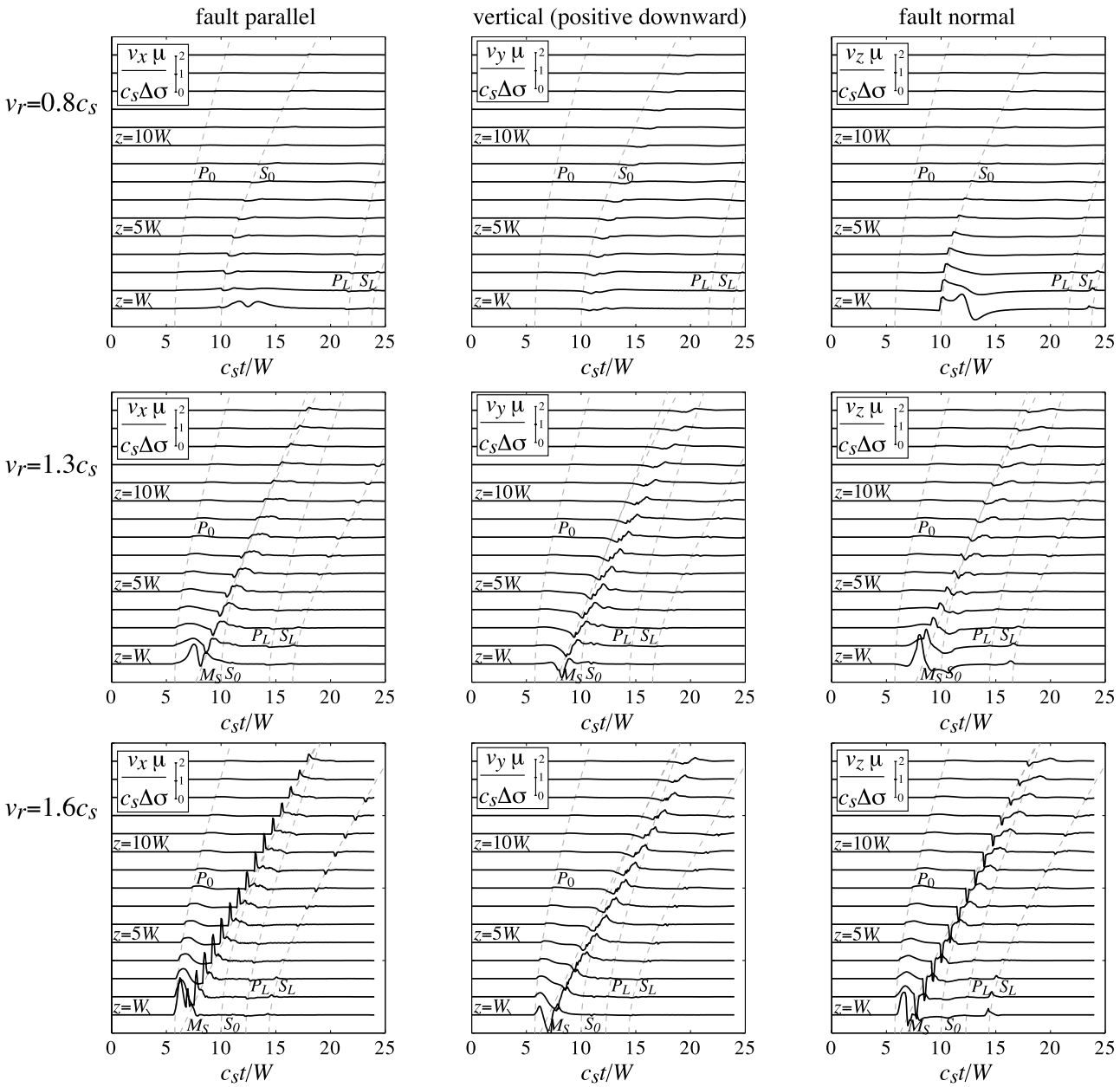

Figure 6. Velocity seismograms at $x = 10\ W$ for various distances from the fault. Major wavefront arrivals are marked. Ruptures have identical G, $\tau_p - \tau_r$, and D_c but different $\Delta\sigma$. Note that the value of $\Delta\sigma$ used to nondimensionalize the velocities is different for each rupture speed (see Table 1).

reference solutions to which we can compare our 3D results to isolate the effects of the finite fault width. The immediately arising question is which parameters should be held fixed when comparing sub-Rayleigh and supershear ruptures. For expanding ruptures on homogeneous faults, the seismic S ratio determines whether or not ruptures will achieve supershear speeds *Andrews* [1976]. While this parameter has less importance in the context of our constant-speed models, this knowledge motivates our method of comparing sub-Rayleigh and supershear ruptures.

[15] Consider the case that both G and $\tau_p - \tau_r$ are intrinsic properties of the fault, which immediately implies a particular D_c as defined above. Then what determines whether or not a rupture propagates at a supershear speed is the stress drop, $\Delta\sigma$, relative to $\tau_p - \tau_r$. From this perspective, we wish to hold G, $\tau_p - \tau_r$, and D_c fixed while varying v_r and $\Delta\sigma$. However, the former quantities all vary with propagation distance in our model. In the 2D self-similar case, G increases linearly with distance [*Broberg*, 1960; *Freund*, 1998; *Broberg*, 1999]. Upon introducing a slip-weakening zone with characteristic size $\Delta\sigma/A$, self-similarity is lost and both $\tau_p - \tau_r$ and D_c become increasing functions of distance. A strictly self-similar model (which would feature a constant $\tau_p - \tau_r$ and a D_c that increased linearly with time or propagation distance) could be achieved by making A inversely proportional to time, but

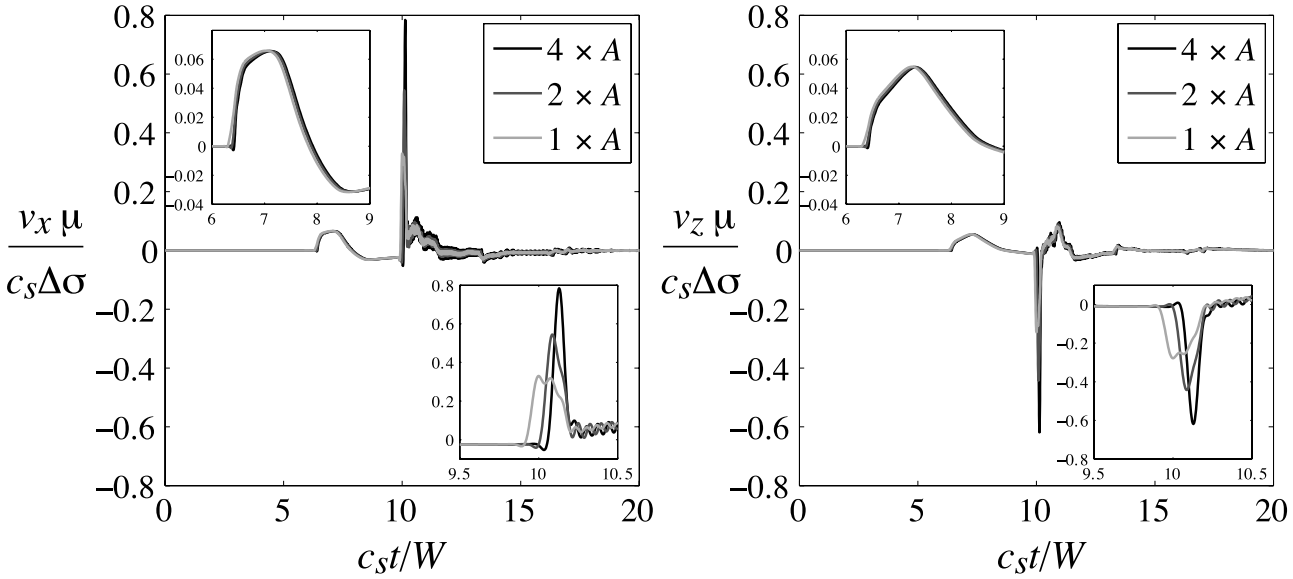

Figure 7. Velocity seismograms at $x = 10\ W$ and $z = 5\ W$ for a supershear rupture ($v_r = 1.6\ c_s$) illustrating the effect of increasing A, the rate of weakening with distance from the rupture front [$A = (\tau_p - \tau_r)/R$] by simultaneously decreasing the cohesive-zone size R and increase the strength drop $\tau_p - \tau_r$. The two insets show close-up views of the dilatational waveform, which is insensitive to A, and the Mach fronts, which are highly sensitive to A. Seismograms at the same location from a sub-Rayleigh rupture with $v_r = 0.8\ c_s$ (not shown), like the dilatational waveform of the supershear rupture, are insensitive to A. Because of the limited numerical resolution in our simulations, we are unable to use realistic values of R, as predicted by *Rice et al.* [2005], and are unable to separate the effects of the shear and Rayleigh Mach fronts.

we do not follow this approach. Instead, we simply select a distance $x^* = 8$ and match G and $\tau_p - \tau_r$ at this location. Matching G at any location suffices to match G for all locations, but this is unfortunately not the case for $\tau_p - \tau_r$ and D_c as discussed above.

[16] The single tunable parameter in our models is A^*, and we first examined the sub-Rayleigh case ($v_r = 0.8\ c_s$) with an eye on numerical resolution. Choosing $A^* = 7.00$ places a minimum of $(\Delta\sigma^*/A^*)/h^* \approx 7$ grid points within the slip-weakening zone; this number increases as the rupture expands (see Figure 3 for an example of our resolution). By gathering data from ruptures with various A^* at the two supershear values of v_r, we identified the model parameters listed in Table 2

[17] We further need to explore how the particular choice of A (and hence $\tau_p - \tau_r$ and D_c) influences field amplitudes. There is considerable uncertainty in the appropriate values of $\tau_p - \tau_r$ and D_c. From the perspective of seismic inversions, here are two primary reasons for this. First, slip inversions are limited in bandwidth, and *Guatteri and Spudich* [2000] and *Spudich and Guatteri* [2004] have shown that a strong trade-off exists between strength drop and slip-weakening distance for sub-Rayleigh ruptures. Second, *Dunham and Archuleta* [2005] have pointed out that, at least for 2D steady state ruptures, the wavefield of sub-Rayleigh ruptures consists entirely of evanescent waves. This implies that a given frequency component of the wavefield decays exponentially with distance from the fault over a scale that is inversely proportional to the frequency. This also occurs for the dilatational component of fields from supershear ruptures. In contrast to this, the frequency content of the shear component of the wavefield (appearing as the Mach waves) is preserved with increasing distance from the fault. To explore this issue in the context of our 3D rupture model, we conduct an additional two runs for $v_r = 0.8$ and $1.6\ c_s$, increasing A first by a factor of two and then by a factor of four.

3. Results

[18] We proceed by propagating ruptures using the model parameters listed in Table 2 for both the 2D and 3D geometries. Prior to examining the off-fault fields, it is appropriate to examine the pattern of wavefronts generated by a bilaterally expanding supershear rupture that stops (discussed here in the 2D context, although a similar pattern appears in 3D as well). Only a certain region, a trapezoid on each side of the fault, experiences the passage of the Mach waves (Figure 4), and it is within this region that the largest amplitudes are expected. In the 2D case, after the rupture has stopped, amplitudes at the planar Mach front remain undiminished as it radiates from the fault.

[19] Figure 5 shows snapshots of particle velocities from our 3D ruptures. The wavefronts illustrated in Figure 4 are clearly seen. As previous studies have revealed, the dominant component of motion changes from the fault-normal to the fault-parallel direction as the rupture exceeds the S-wave speed [*Aagaard and Heaton*, 2004; *Dunham and Archuleta*, 2005]. The two-sided fault-normal pulse dominates the ground motion from sub-Rayleigh ruptures, but the largest amplitudes are concentrated within a distance $\sim W$ from the fault. Large amplitudes are also present in the region beyond the end of the fault; these are carried by S-wave stopping phases. For supershear ruptures, the largest amplitudes,

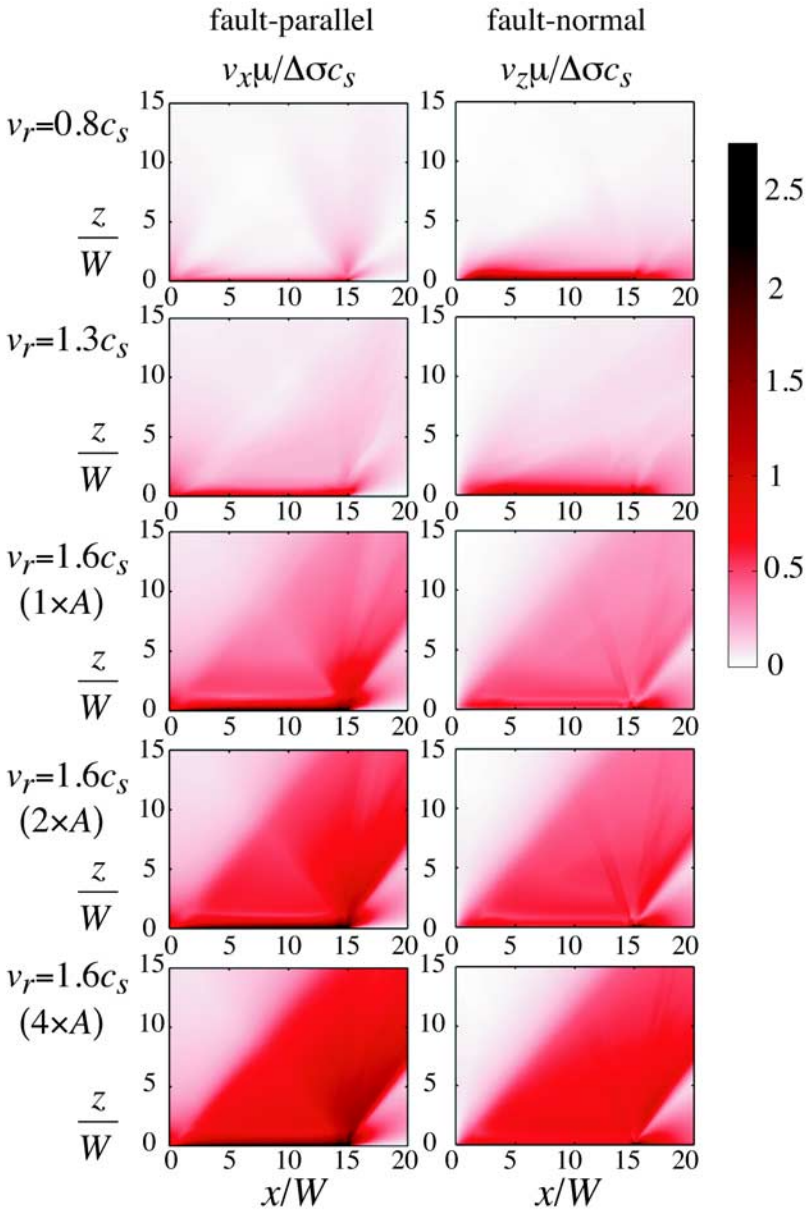

Figure 8. Maximum peak-to-peak amplitude of the free-surface velocity field. The top three rows compare ruptures with different speeds; these ruptures have identical G, $\tau_p - \tau_r$, and D_c but different $\Delta\sigma$. The bottom two rows illustrate the effect of increasing the weakening rate, A, at the rupture front. Fracture energy is preserved, so increasing A increases $\tau_p - \tau_r$ and decreases D_c. For a precise definition of A in our model, see equation (1). Note that the value of $\Delta\sigma$ used to nondimensionalize the velocities is different for each rupture speed (see Table 1). The color scale covers the entire range of amplitudes for the top three rows, but is saturated for the bottom two rows.

aside from those in the immediate vicinity of the rupture front, occur along the closely coincident Rayleigh and shear Mach fronts, which extend from the fault out to a distance determined by how far the rupture has propagated.

[20] To further explore the ground motion histories, we plot seismograms at $x = 10\ W$ for various distances from the fault (Figure 6). The location $x = 10\ W$ is chosen because the rupture is well-developed at this point (in the sense that the effects of the fault width are established), but the effects of the stopping phases are relatively minor. In addition to the seismograms, we mark the arrival times of the P- and S-wave starting and stopping phases and, for stations within the Mach region for supershear ruptures, the Mach front. For example, the S-wave stopping phase arrives at

$$t = \frac{L}{v_r} + \frac{\sqrt{(L-x)^2 + z^2}}{c_s}. \tag{4}$$

The shear Mach front arrives at

$$t = \frac{x + z\sqrt{v_r^2/c_s^2 - 1}}{v_r}, \tag{5}$$

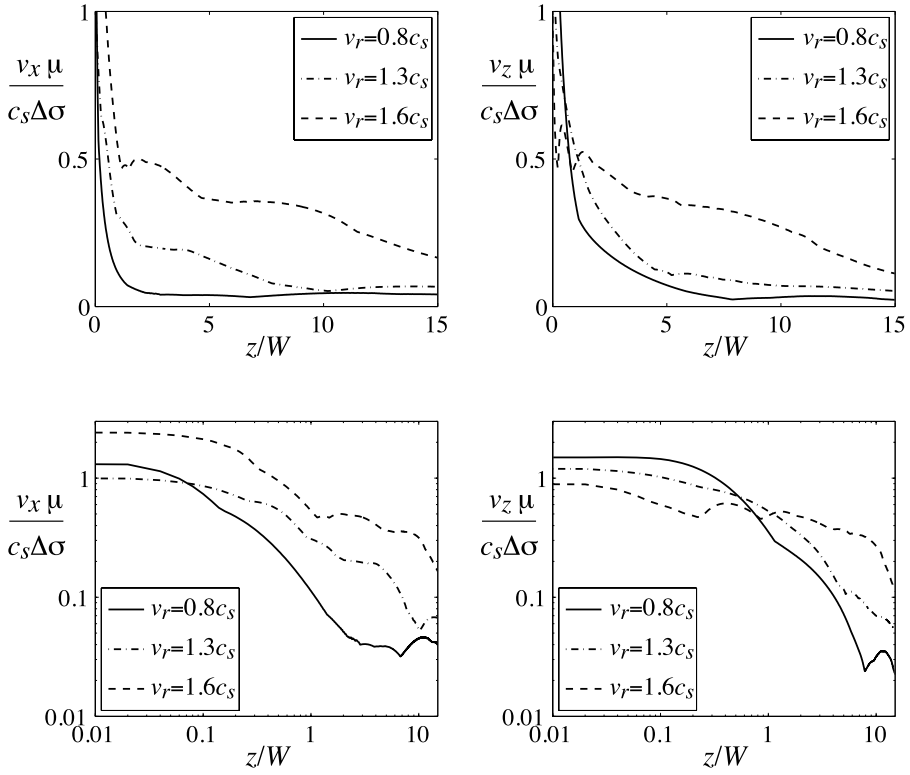

Figure 9. Maximum peak-to-peak amplitude of fields at $x = 10W$ as a function of fault-normal distance (shown on both linear and log-log scales). Ruptures have identical G, $\tau_p - \tau_r$, and D_c, but different $\Delta\sigma$. Note that the value of $\Delta\sigma$ used to nondimensionalize the velocities is different for each rupture speed (see Table 1).

and the Rayleigh Mach front arrives at

$$t = \frac{x + z\sqrt{v_r^2/c_R^2 - 1}}{v_r}, \tag{6}$$

where c_R is the Rayleigh speed.

[21] Using these seismograms as a reference, we are now in a position to determine the influence of the cohesive-zone size on ground-motion amplitudes. To illustrate the main result, we compare velocity seismograms from both sub-Rayleigh and supershear ruptures with three values of A (Figure 7). For supershear ruptures, as A is increased (corresponding to more rapid weakening with a larger $\tau_p - \tau_r$ and smaller D_c but fixed G), amplitudes rise accordingly, but only at the Mach fronts. This is clearly evident when comparing the amplitudes of the dilatational waveform that precedes the Mach fronts; these amplitudes are completely insensitive to how rapidly the fault weakens. It further follows that the entire wavefield (both dilatational and shear components) of sub-Rayleigh ruptures will be rather insensitive to details of the weakening process at the rupture front, and our simulations (not shown) confirm this. A possible exception to this might occur when the rupture process is highly unsteady. If this is the case, then the wavefield would consist of both evanescent and radiating waves; the radiating waves will transport high-frequency signals away from the fault.

[22] Our next step is to quantify the ground motion in our simulations by plotting the maximum peak-to-peak velocity experienced at each point on the free surface (Figure 8). In all cases, the largest ground motion occurs in the immediate vicinity of the fault. For sub-Rayleigh ruptures, the region beyond the fault end in the propagation direction also experiences strong shaking; this is carried by the S-wave stopping phase. For supershear ruptures, locations within the Mach region also experience large amplitudes; this is most evident for $v_r = 1.6\ c_s$. As discussed above, the peak amplitudes transmitted along the Mach front are quite sensitive to the particular details of the weakening process at the rupture front. As A is increased, the amplitudes within the Mach region also increase and eventually dominate any peak-to-peak motion generated by stopping phases.

[23] The final step in our analysis is to plot maximum peak-to-peak amplitudes on the free surface along a line normal to the fault at $x = 10\ W$ (Figure 9). Amplitudes from the supershear rupture with $v_r = 1.6\ c_s$ are almost always the largest, except that fault-normal motion close to the fault is largest from sub-Rayleigh ruptures. The contrast between supershear and sub-Rayleigh ruptures is quite prominent at distances exceeding W. The nonmonotonic decrease of amplitude with increasing distance that appears for supershear ruptures (e.g., around $x = 2\ W$ for $v_r = 1.6\ c_s$ on the fault-parallel component) stems from the fact that close to the fault, peak amplitudes occur not at the Mach fronts but within the dilatational waveform preceding it. At a distance

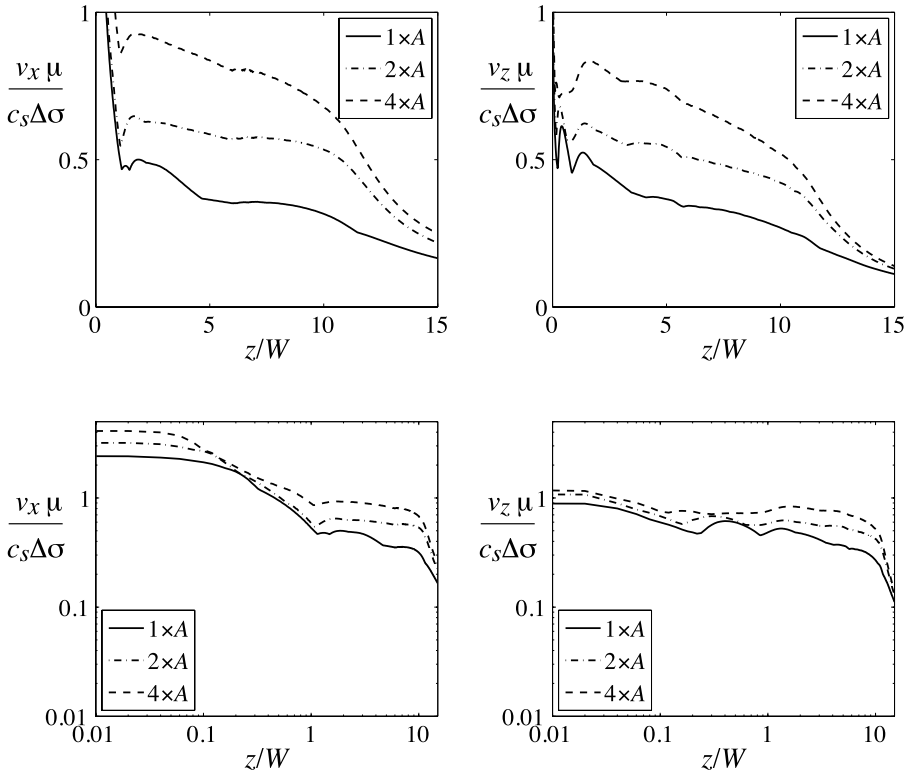

Figure 10. Maximum peak-to-peak amplitude of fields from a supershear rupture ($v_r = 1.6\ c_s$) at $x = 10\ W$ as a function of fault-normal distance (shown on both linear and log-log scales). The weakening rate at the rupture front, A, is increased by a factor of two and then by a factor of four. Fracture energy is preserved, so increasing A increases $\tau_p - \tau_r$ and decreases D_c. For a precise definition of A in our model, see equation (1).

of about 2 W, the Mach waves, which decays at a more gradual rate than dilatational field components, become the carriers of the peak amplitudes. This can be seen by examining the seismograms in Figure 6.

[24] We also show a similar plot for supershear ruptures ($v_r = 1.6\ c_s$) with larger values of A (corresponding to larger $\tau_p - \tau_r$ and smaller D_c) in Figure 10. As A is increased, the Mach fronts become more concentrated and exhibit larger amplitudes. As discussed previously, fields from sub-Rayleigh ruptures become progressively more insensitive to A away from the fault. This means that larger values of A will result in an increase in peak-to-peak amplitudes far from the fault for supershear rupture (as evidenced by Figure 10). On the other hand, sub-Rayleigh ruptures will have amplitudes only as large as those shown in Figure 9 regardless of the extent of the slip-weakening zone. The lack of seismological constraints on the extent of the slip-weakening zone renders it impossible to state precisely the differences in amplitudes of ground motion produced by sub-Rayleigh and supershear ruptures.

[25] As stated earlier, one objective of this project is to evaluate the validity of using the 2D steady state slip-pulse model of *Dunham and Archuleta* [2005] and *Bhat et al.* [2007] to predict fields around propagating ruptures. We consider only the case of $v_r = 1.6\ c_s$, since we are primarily interested in how rapidly amplitudes at the Mach front decay with distance from the fault (which we expect to be influenced by the finite fault width). The parameters of the slip-pulse model are the rupture speed v_r, the strength drop $\tau_p - \tau_r$, the extent of the slip-weakening zone, and the length of the slip pulse. We assign these parameters by matching our 3D results at the free surface when the rupture front reaches $x = 10\ W$. This is shown in Figure 11. Then, by evaluating the expressions given in *Dunham and Archuleta* [2005], we obtain plots of the maximum peak-to-peak amplitudes in the 2D model as a function of distance from the fault; these are compared to our 3D results, calculated not over all time as before, but now from the wavefield present at the time that the rupture front reaches $x = 10\ W$. This appears in Figure 12. The 2D model provides an accurate prediction of the fields in the immediate vicinity of the fault, especially on the fault-parallel component. The fault-normal component is not precisely matched; this is likely because of free surface effects (since the agreement between the two models increases if the station is situated below the free surface). The 2D approximation breaks down at distances larger than W, where an inverse square-root decay of amplitudes at the shear Mach fronts diminishes amplitudes below that in the 2D model. Furthermore, Rayleigh Mach waves are completely absent in the 2D model, and at great distances from the fault, these are expected to carry the largest amplitudes.

4. Numerical Evidence for Rayleigh-Wave Mach Fronts from Supershear Ruptures

[26] The most distinctive feature of the 2D supershear slip-pulse models is the shear Mach wave. In 3D calculations incorporating a free surface, we also expect Mach

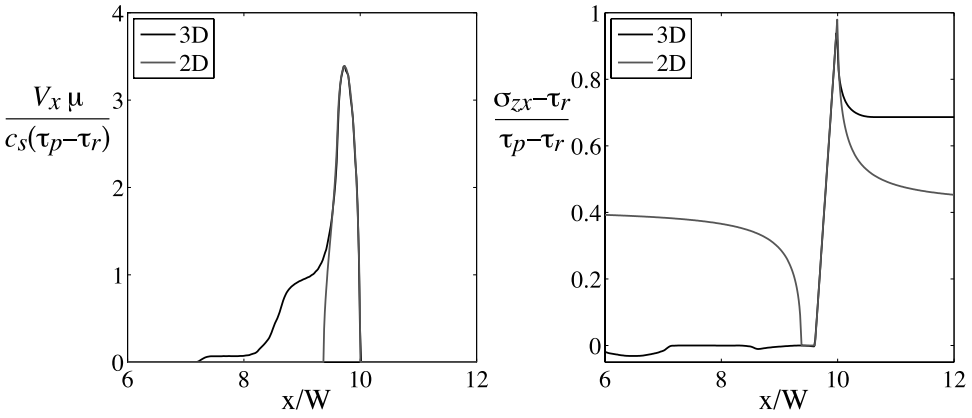

Figure 11. Slip velocity and shear stress for a 3D supershear rupture (v_r = 1.6 c_s) and its approximation by a two-dimensional steady state slip pulse. Parameters are matched to the solution on the fault at the free surface when the rupture reaches x = 10 W.

fronts from Rayleigh waves that are generated by the interaction of the rupture with the surface. As a rupture propagates through an elastic half-space it would, if constraints of plane strain in the $x - z$ plane were imposed, perturb the out-of-plane stress component, σ_{yy}, near the free surface. Since there is nothing to supply such constraints, σ_{yy} must vanish on the free surface; this can be accomplished by applying moving normal loads on the surface to negate the otherwise nonzero σ_{yy} pattern. These loads, which propagate at a super-Rayleigh speed if the rupture speed is supershear, will then excite Rayleigh Mach waves [*Lansing*, 1966; *Georgiadis and Lykotrafitis*, 2001].

[27] As our simulations reveal, supershear slip pulses emit both Rayleigh and shear Mach waves into Mach bands bounded by linear wavefronts extending from both the leading and trailing edges of the slipping region, though the largest amplitudes occur in a narrower region corresponding to the portion of the slip pulse having the largest slip velocities (typically the size of the slip-weakening zone). The Rayleigh and shear Mach bands overlap close to the fault, but since the Rayleigh-wave speed is less than the S-wave speed, the two Mach bands eventually separate at sufficiently far distances from the fault. Denoting the length of the region emitting strong Mach waves as $\tilde{R}$, the two Mach bands separate at the fault-normal distance of

$$z = \tilde{R}/(\cot\beta_R - \cot\beta_s), \tag{7}$$

where β_R = arcsin (c_R/v_r) and β_s = arcsin (c_s/v_r) are the angles between the $-x$-axis and the Rayleigh and shear Mach fronts (or, equivalently, the half-angle of the Mach cones). The difficulty in clearly distinguishing the Rayleigh and shear Mach waves arises from the fact that the angle of the Rayleigh Mach fronts is only slightly smaller than that of the shear Mach fronts. For v_r = 1.6 c_s and $c_R \approx 0.9194\ c_s$ (assuming a Poisson material), $\beta_s - \beta_R \approx 3.6°$ and the separation distance is $z \approx 5.7\ \tilde{R}$.

[28] The Rayleigh and shear Mach bands overlap over the entire computational domain in our simulations, but this may be an artifact of the extremely large slip-weakening zones (several kilometers when dimensionalized) that we had to assume to make our simulations numerically feasible. This is vastly larger than the estimate by *Rice et al.* [2005] of a few tens of meters. If their estimates are indeed correct, then the Rayleigh and shear Mach bands will separate at a fault-normal distance much smaller than W.

[29] Since the orientation of the two Mach bands is so similar, we confirm the existence of the Rayleigh Mach waves by exploiting certain properties of the particle velocities and stresses. First, we separate the dilatational and shear components of the fault-parallel and fault-normal velocities. To isolate the dilatational field, we take the divergence of the velocity vector. This filters out the shear component of the velocity (though it only approximately removes all S waves since S waves impinging on the free surface can generate both P and Rayleigh waves). The resulting Mach band associated with this filtered field should be parallel to the expected orientation of the Rayleigh Mach front. To isolate the shear contribution to the velocity field, we take its curl and approximately filter out

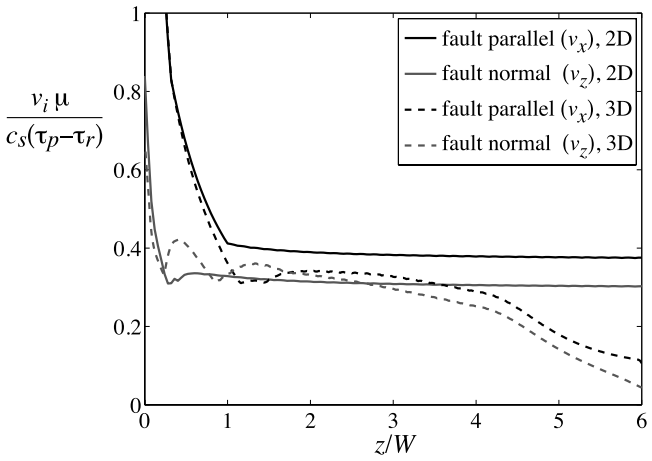

Figure 12. Maximum peak-to-peak amplitude of fields when the rupture reaches x = 10 W as a function of fault-normal distance. The curves labeled "3D" are from our three-dimensional numerical simulations (stations on the free surface); these are compared with the two-dimensional steady state slip-pulse model (labeled "2D") of *Dunham and Archuleta* [2005] and *Bhat et al.* [2007].

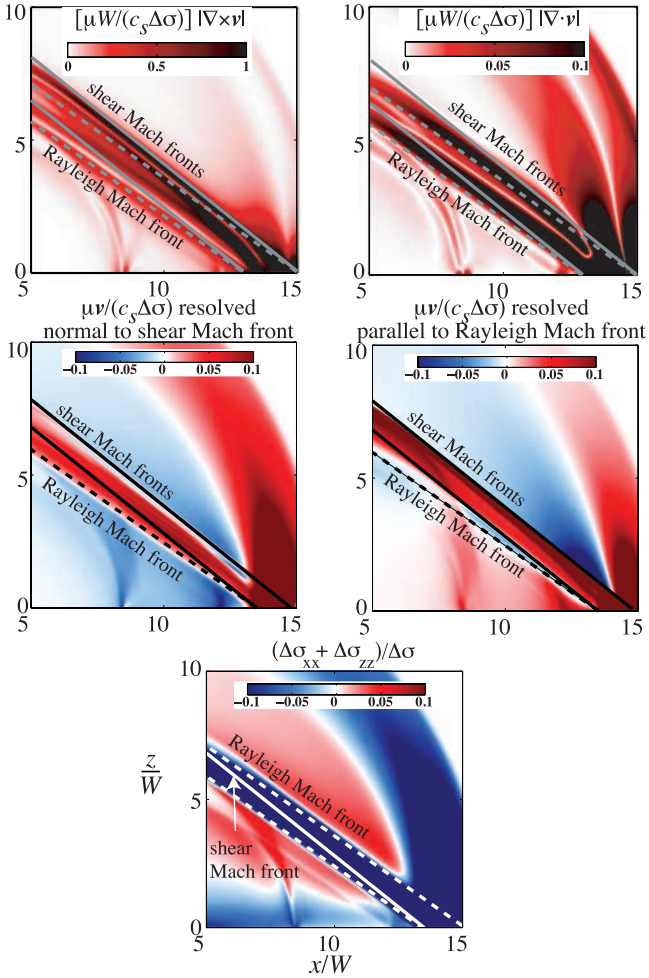

Figure 13. Various filtering techniques adopted to separate the Rayleigh and shear Mach fronts on the free surface (shown for the case of $v_r = 1.6\ c_s$). The solid lines are the shear Mach fronts and the dashed lines are the Rayleigh Mach fronts. $\nabla \cdot \mathbf{v}$ filters out shear contributions, and $\nabla \times \mathbf{v}$ filters out dilatational contributions (note that Rayleigh waves are comprised of both shear and dilatational fields). $\mathbf{v}$ resolved normal to the shear Mach front isolates Rayleigh Mach waves, and $\mathbf{v}$ resolved parallel to the Rayleigh Mach front isolates shear Mach waves. $\Delta\sigma_{xx} + \Delta\sigma_{zz}$ (which is the trace of the stress change tensor since $\sigma_{yy} = 0$ on the surface) is zero in the shear Mach band, but will be nonzero within the Rayleigh Mach band.

P waves and the dilatational component of Rayleigh waves. The resulting Mach band of the filtered field is parallel to the shear Mach front orientation. The filtered fields are shown in Figure 13. The curl and divergence are computed using finite differences in the $x - z$ plane (free surface) only; partial derivatives with respect to y are converted to partial derivatives with respect to x and/or z by exploiting the fact that $\sigma_{yx} = \sigma_{yy} = \sigma_{yz} = 0$ on the free surface. For example, since $\sigma_{yx} = \mu\ (\partial u_x/\partial y + \partial u_y/\partial x) = 0$, then (after taking the time derivative), $\partial v_x/\partial y = -\partial v_y/\partial x$. We have also smoothed the data for this figure to remove oscillations arising from the dispersive nature of the numerical method, which are further compounded by numerical differentiation.

[30] Second, the surface velocity vector associated with shear Mach waves should be parallel to the shear Mach front, and the velocity vector associated with Rayleigh Mach waves should be perpendicular to the Rayleigh Mach front. Thus the component of velocity parallel to the Rayleigh Mach front should isolate the shear Mach band, and the component of velocity normal to the shear Mach front should isolate the Rayleigh Mach band. Figure 13 shows this. In general we notice that the Rayleigh Mach waves are largest toward the trailing edge of the Mach band and that the shear Mach waves are largest toward the leading edge.

[31] A third way to illustrate the existence of Rayleigh Mach waves is to look at the volumetric part of the stress field. For a 2D plane-strain supershear rupture, the Mach waves are entirely composed of S waves. This means that the volumetric part of the stress tensor (i.e., the trace, $\Delta\sigma_{xx} + \Delta\sigma_{yy} + \Delta\sigma_{zz}$) vanishes within the Mach band. In 3D, if the Mach band is composed mainly of S waves, then the same condition should be true. We check for this feature in our 3D results on the free surface (where $\Delta\sigma_{yy} = 0$), and as Figure 13 demonstrates, this is clearly not the case. In fact we see large compressive stressing in the Mach band, which is consistent with the expected sense of stressing due to a Rayleigh wave that exerts compressional stresses in both the fault-parallel and fault-normal directions on the compressional side of the fault. Furthermore, the Mach band revealed in this filtered field is cleanly delimited by the Rayleigh Mach fronts.

[32] We also conducted a simulation at $v_r = \sqrt{2}\ c_s$. At this speed, no S waves are excited (at least in two-dimensional models). Our simulation results (not shown) confirm that Rayleigh Mach waves are excited by ruptures propagating at $v_r = \sqrt{2}\ c_s$. These Mach waves have exactly the properties that were identified using the various filtering techniques discussed above.

[33] We have thus shown that unlike the 2D supershear slip-pulse models of *Dunham and Archuleta* [2005] and *Bhat et al.* [2007], in which the Mach band was composed solely of S waves, supershear ruptures in a 3D elastic half-space also generate Rayleigh Mach waves. This leads to a more complex stress and velocity field within the Mach bands. Most importantly, since Rayleigh waves are confined to the free surface, they experience less attenuation from geometrical spreading. In fact, for the ideally elastic medium we consider here, Rayleigh Mach waves will suffer no attenuation with distance from the fault. This leads us to expect that even in 3D, supershear ruptures are capable of transmitting significant ground motion and stresses beyond distances comparable to the fault width.

5. Off-fault Stressing and Activation of Secondary Faults

[34] We next turn our attention to the off-fault stress fields, in particular to explore the hypothesis that the large stresses carried by the shear and Rayleigh Mach waves of supershear ruptures could activate secondary faulting on nearby faults. The observation of triggered faulting in the 2002 Denali fault earthquake [*Eberhart-Phillips et al.*, 2003] prompted studies of whether or not something similar could occur in southern California [*Anderson et al.*, 2003].

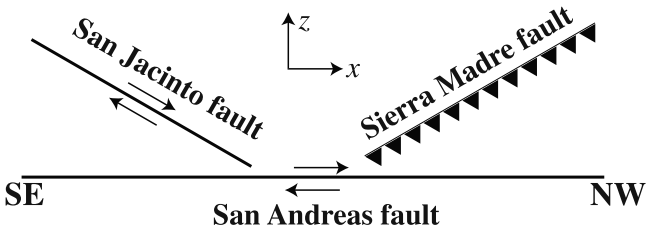

Figure 14. Geometry of faults on which Coulomb stress change, ΔCS, is calculated. The right-lateral vertical strike-slip (San Jacinto-like) and thrust (Sierra Madre-like) faults strike at 150° and 30°, respectively, with respect to the main (San Andreas-like) fault. The Sierra Madre-like fault dips at 30°. Note that only the fault plane orientations are required to calculate ΔCS; hence the location and dimensions of the faults are for illustrative purposes only.

Our work builds on the latter study, though we do not permit slip to occur on secondary faults. Instead, we look at Coulomb stress changes, ΔCS, on pre-existing fault structures of a given orientation (Figure 14). We specifically focus on two fault orientations, motivated by potential rupture of the southern San Andreas fault. The first is a thrust fault with a dip of 30° that strikes at 30° with respect to the main fault, which provides a rough approximation to thrust features like the Sierra Madre fault north of the Los Angeles basin. The second is a vertical strike-slip fault that strikes at 150° with respect to the main fault. This orientation is inspired by the San Jacinto fault; like the main fault, it is right-lateral. Note that we do not specify any spatial dimensions of the faults as we are only interested in resolving shear and normal stresses onto structures of a particular orientation. The precise procedure for calculating Coulomb stress changes is given in Appendix A. To briefly summarize the procedure, we calculate the shear stress change in the direction of slip, $\Delta\tau$, and the normal stress change, $\Delta\sigma_n$ (positive in tension), and then evaluate $\Delta CS = \Delta\tau + f_s\,\Delta\sigma_n$ for a static friction coefficient of $f_s = 0.6$. Finally, it is important to keep in mind that these estimates are surely affected by our large slip-weakening zone sizes, which cause the high-stress shear and Rayleigh Mach fronts to remain overlapped in the computational domain (they do not seem to have reinforcing effects on Coulomb stress in general, but rather seem to have somewhat opposing effects).

[35] Figures 15 and 16 show snapshots from our 3D simulations of ΔCS, evaluated at mid-seismogenic depth ($y = 0.5\ W$) at two times: just as the rupture arrives the edge of the fault and at a slightly later time (an additional 3 W/c_s after the arrival) to emphasize the stopping phases. Stress fields are evaluated at every point on the free surface, and only the regions of positive Coulomb stress change ($\Delta CS > 0$) are shown. While *Bhat et al.* [2007] have obtained simple expressions for the far-field stress perturbation along the shear Mach band of a 2D supershear slip pulse, any comparison of their results with the 3D calculations would be invalid as the dilatational part of the stress field in the Mach bands is non-negligible. A possible exception might occur at distances sufficiently removed from the fault that

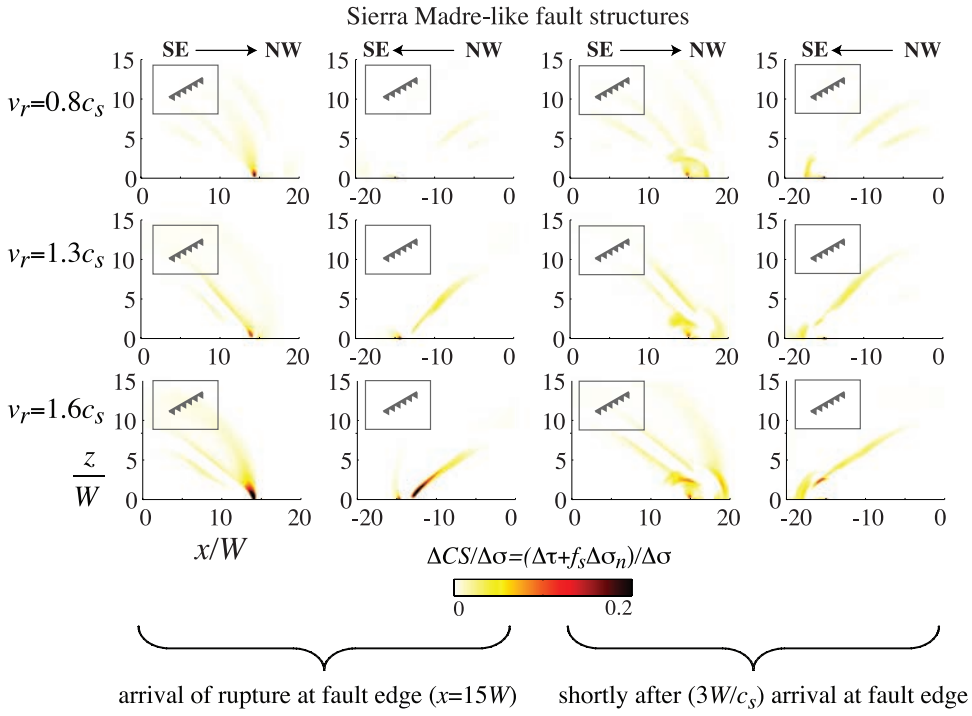

Figure 15. Snapshots of Coulomb stress change, ΔCS, on Sierra Madre-like thrust structures at mid-seismogenic depth ($y = 0.5\ W$) for various ruptures speeds at two times: just as the rupture arrives the edge of the fault and at a slightly later time (an additional 3 W/c_s after the arrival) to emphasize the stopping phases. Ruptures have identical G, $\tau_p - \tau_r$, and D_c but different $\Delta\sigma$. Note that the value of $\Delta\sigma$ used to nondimensionalize the velocities is different for each rupture speed (see Table 1).

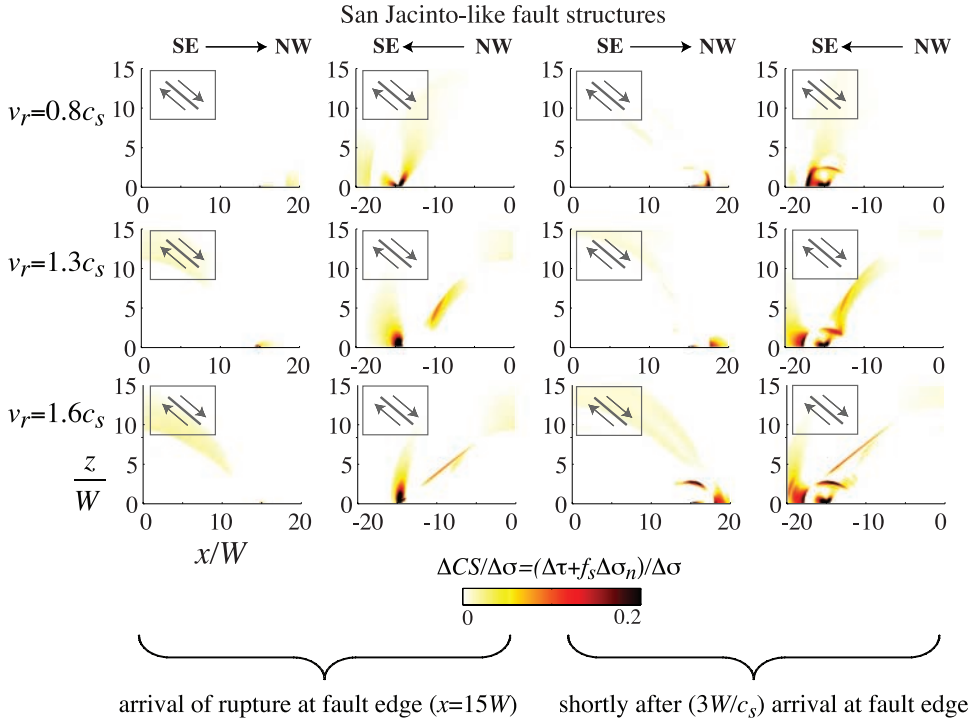

Figure 16. Same as Figure 15 but for San Jacinto-like strike-slip structures.

shear and Rayleigh Mach bands do not overlap (such distances are probably unrealistically large in our simulations). Furthermore, we emphasize that the figures would likely look notably different if calculations could be done with small enough slip-weakening zones that the shear and Rayleigh Mach bands did not overlap so substantially as in the present work.

[36] Figure 15 shows ΔCS for Sierra Madre-like structures due to a rupture propagating at various speeds and propagation directions on a San Andreas-like fault. In general, these thrust structures are favorably oriented for activation by stresses within the Mach bands of supershear ruptures ($v_r > \sqrt{2}\, c_s$) propagating from the northwest (NW) to the southeast (SE) on San Andreas. The fault structures strike almost parallel to the Mach fronts for this direction of propagation. For SE to NW propagation, Sierra Madre-like structures are favorably stressed for activation (for both v_r = 0.8 c_s and 1.6 c_s), but these stress changes are smaller than those from supershear ruptures propagating NW to SE. The influence of propagation direction is even more pronounced for San Jacinto-like structures, as illustrated in Figure 16. For all speeds, the favorable propagation direction for activation of these strike-slip structures is from the NW to the SE. In this case, the fault structures strike almost perpendicular to the Mach fronts.

[37] It is interesting to note that the radiated stress field from stopping a supershear rupture at v_r = 1.6 c_s is only slightly larger than that from stopping a sub-Rayleigh rupture. This is due to the fact that as the rupture approaches the P-wave speed, the dilatational field undergoes a Lorentz-like contraction parallel to the propagation direction. Furthermore, we see that the amplitude of Coulomb stress changes at the Mach fronts is generally comparable to stress changes in the immediate vicinity of the fault from a stopping sub-Rayleigh rupture. For a stress drop of 3 MPa, the Coulomb stress perturbation carried by the Mach front for v_r = 1.6 c_s is about 0.3 MPa at a distance of 3 W. This estimate will only increase with decreasing slip-weakening-zone size.

[38] *Harris et al.* [1991], *Harris and Day* [1993] and *Fliss et al.* [2005] suggest that stopping-phase stress fields might activate slip on adjacent, but unconnected, fault segments. However, while the large stress perturbation experienced in the near-fault-end region (for both sub-Rayleigh and supershear ruptures) is a permanent feature (at least until the next earthquake), the Mach-front stress perturbations are transient. The typical duration of this stress (for the probably too-large slip-weakening-zone sizes in our simulations) at a distance of 5 W is about 0.5 W/c_s, which translates to about 1.7 seconds for representative values of W and c_s. It is not yet established whether or not stress perturbations of such short duration (but large amplitude) can nucleate ruptures on secondary faults.

[39] Figure 17 shows the maximum positive Coulomb stress change, $\Delta CS_{\max}$, experienced over all times at locations along a line extending from the fault at x = 10 W and y = 0.5 W. The direction of propagation for sub-Rayleigh ruptures barely changes $\Delta CS_{\max}$ in the far field ($z \gg W$) experienced by our two secondary fault orientations. For supershear ruptures, the propagation direction that favors activation of San Jacinto-like and Sierra Madre-like ruptures is clear. A NW to SE supershear rupture transmits stresses along the Mach front out to distances as large as our computational domain (15 W) that might activate San Jacinto-like faults. For Sierra Madre-like thrust features, SE to NW propagation produces the largest stresses, though propagation in the opposite direction also generates significant stresses. Finally, these estimates of stress changes from

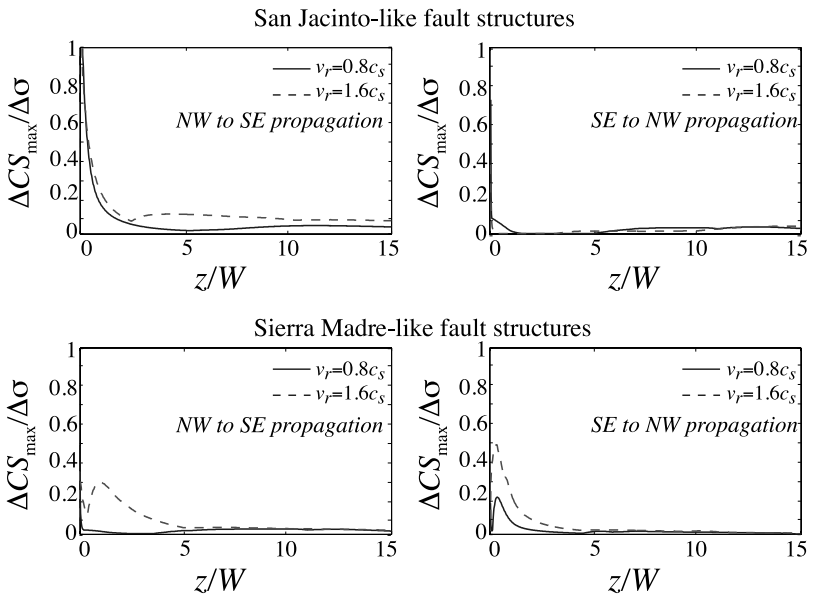

Figure 17. Evolution of maximum positive Coulomb stress change, $\Delta CS_{\max}$, on San Jacinto-like and Sierra Madre-like fault structures with fault-normal distance. $\Delta CS_{\max}$ is evaluated at $x = 10\ W$ at mid-seismogenic depth ($y = 0.5\ W$).

supershear ruptures are highly sensitive to details of the weakening process at the rupture front, as discussed earlier in the context of the velocity field. The estimates given here should be interpreted as a lower bound, since we are constrained to the most gradual of physically likely weakening rates by numerical constraints. When parametrized by the slip-weakening distance, a reduction of D_c from about 2 m (as used in the calculations shown here) to 0.5 m (with a corresponding increase in the strength drop) would increase amplitudes at the Mach fronts by a factor of four. Furthermore, the overlapping Mach bands are sometimes partly self-canceling as regards contributions to ΔCS, a feature that would not be present when they do not overlap.

6. Discussion

[40] We have explored the influence of rupture speed on the character and amplitude of ground motion and radiated stresses from ruptures on a vertical finite-width fault breaking the free surface of a half-space. This extends our previous work on supershear dynamic ruptures in two dimensions [*Dunham and Archuleta*, 2005; *Bhat et al.*, 2007]. In those 2D steady state models, shear Mach waves transport velocities and stresses comparable to those experienced on the fault out to infinity. Without a source of waves below the bottom edge of the fault, field amplitudes in our 3D model must diminish beyond a distance that scales with the fault width, W (the exception being Rayleigh Mach waves on the free surface). As *Ben-Menahem and Singh* [1987] pointed out, the decay rate of shear Mach waves will be governed by the geometrical spreading of the Mach cone, causing amplitudes to decrease with the inverse square-root of distance from the fault. In addition to producing the shear Mach waves seen previously in 2D models, 3D supershear ruptures in a half-space also generate Rayleigh Mach fronts, which are present even if the rupture propagates at $\sqrt{2}\ c_s$. These factors lead to more complex velocity and stress fields within the Mach bands. The same geometrical spreading considerations suggest no attenuation of Rayleigh Mach waves.

[41] We have not modeled two important factors that will influence field amplitudes: incoherence of the rupture process, and scattering and attenuation along the path of radiating waves. The former has been examined by *Bernard and Baumont* [2005] in the context of rupture-front curvature. At distances much closer than W, an extra factor proportional the inverse square-root of distance to the fault must be added. *Ben-Menahem and Singh* [1987] accounted for attenuation in the form of a constant quality factor in their study of propagating supershear dislocations, finding the precise manner in which attenuation bounds otherwise infinite accelerations (from their delta-function source time function).

[42] As our 2D models suggested, there are significant differences between the radiated wavefields of sub-Rayleigh and supershear ruptures. Off-fault fields not in the immediate vicinity of the fault are only sensitive to details of the weakening process at the rupture front within the Mach bands of supershear ruptures. Increasing the weakening rate (by simultaneously decreasing the extent of the slip-weakening zone and increasing the strength drop) increases the amplitudes of the Mach waves. In general, we find that supershear ruptures produce larger amplitudes of velocities and stresses far from faults than do sub-Rayleigh ruptures. For W = 10 km, a stress drop of 3 MPa, and a slip-weakening distance of about 2 m, peak velocities of 0.1 m/s are expected at 10 km. Coulomb stress changes (on favorably oriented faults) at these distances are about 1 MPa. Both velocity and stress amplitudes scale linearly with stress drop and, quite importantly, depend also on the extent of the slip-weakening zone. The estimates given above lie at the most conservative end of physically likely values, since much smaller slip-weakening distances (which would generate

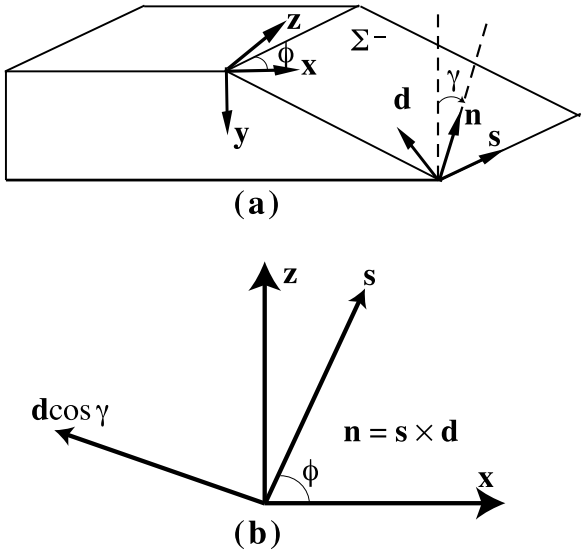

Figure A1. (a) Σ^- side of the fault plane, taken as the footwall for the dipping fault, and chosen arbitrarily if the fault is vertical. **s**, **d**, and **n** are an orthogonal set of unit vectors corresponding to the strike, updip, and outward normal to Σ^-. ϕ is the angle measured from the x-axis to **s**, with positive values indicating a rotation about the y-axis from the positive x-axis toward the positive z-axis. γ is the angle between the vertical and **n**. (b) **s** and the projection of **d** on the $x - z$ plane.

much higher velocities and stresses) have been suggested from a combination of laboratory constraints and seismic observations [*Rice et al.*, 2005]. When decreasing the extent of the slip-weakening zone by some factor, the peak velocities and stresses at the Mach front are increased by approximately that same factor. Without constraints on the extent of the slip-weakening zone, it is impossible to state exactly how much larger ground motion from supershear ruptures will be, compared to that from sub-Rayleigh ruptures.

[43] Our results also raise the possibility that stresses from a supershear rupture might initiate slip on faults adjacent to the one hosting the supershear rupture. As a hypothetical example, we consider what might occur if the southern San Andreas fault fails at supershear speeds. Activation of San Jacinto-like structures is favored if the rupture propagates from the northwest to the southeast, while activation of Sierra Madre-like structures is favored by ruptures propagating in the opposite direction. Our least conservative, but computationally most feasible, parameter choice involves overlap of the two Mach bands at all distances shown, a condition which usually leads to some partial cancellation of Coulomb stress changes that would not be present for more conservative choices when the bands do not overlap except quite near the fault.

Appendix A: Coulomb Stress on Fault Planes of Known Orientation

[44] Consider a fault plane Σ in a 3D space (Figure A1). Let x, y, and z form a right-handed coordinate system where the surface of the earth is in the x–z plane and the y-axis points vertically downward from the earth's surface. The strike direction, **s**, is chosen along the surface trace of the fault plane such that the dip γ, defined below, lies between 0 and 90. **s** makes an angle of ϕ with the x-axis (with positive values indicating a rotation about the y-axis from the positive x-axis toward the positive z-axis). Let Σ^+ and Σ^- to be the positive and the negative sides of the fault plane; Σ^- is the footwall (and is assigned arbitrarily for vertical faults). Let **n** be the unit normal to the fault plane directed from Σ^- to Σ^+. This implies that any traction calculated with respect to this vector represents the action on the Σ^- plane because of the Σ^+ plane. Let γ be the dip of the fault plane, with positive values corresponding to right-handed rotation about **s**.

[45] Looking at Figure A1, the component of **d** in the $x - z$ plane is **d** cosγ. Since this component is perpendicular to **s**, the projections of **d** onto the x- and z-axes are $-\sin\phi\ \cos\gamma$ and $\cos\phi\ \cos\gamma$. Thus

$$\mathbf{d} = -\sin\phi\cos\gamma\mathbf{i} - \sin\gamma\mathbf{j} + \cos\phi\cos\gamma\mathbf{k}. \tag{A1}$$

The unit vector pointing in the strike direction is

$$\mathbf{s} = \cos\phi\mathbf{i} + \sin\phi\mathbf{k}, \tag{A2}$$

and the unit normal is $\mathbf{n} = \mathbf{s} \times \mathbf{d}$ or

$$\mathbf{n} = \sin\phi\sin\gamma\mathbf{i} - \cos\gamma\mathbf{j} - \cos\phi\sin\gamma\mathbf{k}. \tag{A3}$$

[46] The rake angle, λ, is the angle between the unit slip vector, ξ (the slip vector $\Delta\mathbf{u}$ is defined as $\mathbf{u}^+ - \mathbf{u}^-$, where **u** is the displacement vector and $\xi = \Delta\mathbf{u}/|\Delta\mathbf{u}|$) and **s**. Positive values of λ indicate rotations counterclockwise rotation about **n** from **s** to ξ. In terms of the rake angle, the unit slip vector is

$$\xi = \mathbf{s}\cos\lambda + \mathbf{d}\sin\lambda. \tag{A4}$$

A rake angle of 0 or π corresponds to pure left-lateral or right-lateral faulting, and a rake angle of $-\pi/2$ or $\pi/2$ corresponds to pure normal or thrust faulting.

[47] The shear stress on the fault in the slip direction is $\tau = \xi_i\sigma_{ij}n_j$ and the normal stress on the fault plane (positive in tension) is $\sigma_n = n_i\sigma_{ij}n_j$ where σ_{ij} are the components of the stress tensor. τ is positive when slip occurs in the direction of the unit slip vector. That direction is surface parallel for strike-slip faults and in the direction of the dip for dip-slip faults. The Coulomb stress change, *CS*, is given by $CS = \tau + f_s\sigma_n$ where f_s is the static coefficient of friction. We emphasize that this is the *CS* component associated with an assumed slip direction, ξ.

[48] **Acknowledgments.** EMD acknowledges partial support from a Reginald A. Daly Postdoctoral Fellowship at Harvard. This work was also supported by NSF-EAR 0440145 and by the NSF/USGS Southern California Earthquake Center, funded by NSF Cooperative Agreement EAR-0106924 and USGS Cooperative Agreement 02HQAG0008. The SCEC contribution number for this paper is 1086. We thank Jim Rice and Renata Dmowska for insightful discussions and Andreas Plesch for help understanding fault geometry in southern California. We also thank Raúl Madariaga for pointing out to us the possibility of supershear ruptures generating Rayleigh Mach

waves and Michel Bouchon for pointing out that these waves ought to be present even when $v_r = t > \sqrt{2}\, c_s$.

References

Aagaard, B. T., and T. H. Heaton (2004), Near-source ground motions from simulations of sustained intersonic and supersonic fault ruptures, *Bull. Seismol. Soc. Am.*, *94*(6), 2064–2078, doi:10.1785/0120030249.

Anderson, G., B. Aagaard, and K. Hudnut (2003), Fault interactions and large complex earthquakes in the Los Angeles area, *Science*, *302*, 1946–1949, doi:10.1126/science.1090747.

Andrews, D. J. (1976), Rupture velocity of plane strain shear cracks, *J. Geophys. Res.*, *81*(32), 5679–5687.

Andrews, D. J. (1985), Dynamic plane-strain shear rupture with a slip-weakening friction law calculated by a boundary integral method, *Bull. Seismol. Soc. Am.*, *75*(1), 1–21.

Antolik, M., R. E. Abercrombie, and G. Ekström (2004), The 14 November 2001 Kokoxili (Kunlunshan), Tibet, earthquake: Rupture transfer through a large extensional step-over, *Bull. Seismol. Soc. Am.*, *94*(4), 1173–1194, doi:10.1785/012003180.

Archuleta, R. J. (1984), A faulting model for the 1979 Imperial Valley earthquake, *J. Geophys. Res.*, *89*(B6), 4559–4585.

Ben-Menahem, A., and S. J. Singh (1981), *Seismic Waves and Sources*, Springer Verlag, New York.

Ben-Menahem, A., and S. J. Singh (1987), Supershear accelerations and Mach-waves from a rupturing front. part 1. Theoretical model and implications, *J. Phys. Earth*, *35*, 347–365.

Bernard, P., and D. Baumont (2005), Shear Mach wave characterization for kinematic fault rupture models with constant supershear rupture velocity, *Geophys. J. Int.*, *162*(2), 431–447, doi:10.1111/j.1365-246X.2005.02611.x.

Bhat, H. S., R. Dmowska, G. C. P. King, Y. Klinger, and J. R. Rice (2007), Off-fault damage patterns due to supershear ruptures with application to the 2001 Mw 8.1 Kokoxili (Kunlun) Tibet earthquake, *J. Geophys. Res.*, *112*, B06301, doi:10.1029/2006JB004425.

Bouchon, M., and M. Vallée (2003), Observation of long supershear rupture during the magnitude 8.1 Kunlunshan earthquake, *Science*, *301*, 824–826, doi:10.1126/science.1086832.

Bouchon, M., M.-P. Bouin, H. Karabulut, M. N. Toksöz, M. Dietrich, and A. J. Rosakis (2001), How fast is rupture during an earthquake? New insights from the 1999 Turkey earthquakes, *Geophys. Res. Lett.*, *28*(14), 2723–2726.

Bouchon, M., M. N. Toksöz, H. Karabulut, M.-P. Bouin, M. Dietrich, M. Aktar, and M. Edie (2002), Space and time evolution of rupture and faulting during the 1999 Izmit (Turkey) earthquake, *Bull. Seismol. Soc. Am.*, *92*(1), 256–266, doi:10.1785/0120000845.

Broberg, K. B. (1960), The propagation of a brittle crack, *Arkiv Fysik*, *18*, 159–192.

Broberg, K. B. (1999), *Cracks and Fracture*, Academic Press, London.

Burridge, R. (1973), Admissible speeds for plane-strain shear cracks with friction but lacking cohesion, *Geophys. J. Roy. Astr. Soc.*, *35*, 439–455.

Burridge, R., G. Conn, and L. B. Freund (1979), The stability of a rapid mode II shear crack with finite cohesive traction, *J. Geophys. Res.*, *84*(B5), 2210–2222.

Dalguer, L. A., and S. M. Day (2007), Staggered-grid split-node method for spontaneous rupture simulation, *J. Geophys. Res.*, *112*, B02302, doi:10.1029/2006JB004467.

Das, S., and K. Aki (1977), A numerical study of two-dimensional spontaneous rupture propagation, *Geophys. J. Roy. Astr. Soc.*, *50*, 643–668.

Dunham, E. M., and R. J. Archuleta (2004), Evidence for a supershear transient during the 2002 Denali Fault earthquake, *Bull. Seismol. Soc. Am.*, *94*(6B), S256–S268, doi:10.1785/0120040616.

Dunham, E. M., and R. J. Archuleta (2005), Near-source ground motion from steady state dynamic rupture pulses, *Geophys. Res. Lett.*, *32*, L03302, doi:10.1029/2004GL021793.

Eberhart-Phillips, D., et al. (2003), The 2002 Denali fault earthquake, Alaska: A large magnitude, slip-partitioned event, *Science*, *300*, 1113–1118.

Ellsworth, W. L., et al. (2004), Near-field ground motion of the 2002 Denali Fault, Alaska, earthquake recorded at Pump Station 10, *Earthq. Spectra*, *20*(3), 597–615, doi:10.1193/1.1778172.

Eshelby, J. D. (1949), Uniformly moving dislocations, *Proc. Phys. Soc. A*, *62*, 307–314.

Favreau, P., M. Campillo, and R. Iionescu (2002), Initiation of shear instability in three-dimensional elastodynamics, *J. Geophys. Res.*, *107*(B7), 2147, doi:10.1029/2001JB000448.

Fliss, S., H. S. Bhat, R. Dmowska, and J. R. Rice (2005), Fault branching and rupture directivity, *J. Geophys. Res.*, *110*, B06312, doi:10.1029/2004JB003368.

Freund, L. B. (1998), *Dynamic Fracture Mechanics*, Cambridge Univ. Press, Cambridge.

Georgiadis, H. G., and G. Lykotrafitis (2001), A method based on the Radon transform for three-dimensional elastodynamic problems of moving loads, *J. Elast.*, *65*, 87–129, doi:10.1023/A:1016135605598.

Guatteri, M., and P. Spudich (2000), What can strong-motion data tell us about slip-weakening fault-friction laws, *Bull. Seismol. Soc. Am.*, *90*(1), 98–116, doi:10.1785/0119990053.

Harris, R. A., and S. M. Day (1993), Dynamics of fault interaction: Parallel strike-slip faults, *J. Geophys. Res.*, *98*(B3), 4461–4472.

Harris, R. A., R. J. Archuleta, and S. M. Day (1991), Fault steps and the dynamic rupture process: 2-D numerical simulations of a spontaneously propagating shear fracture, *Geophys. Res. Lett.*, *18*(5), 893–896.

Kristek, J., P. Moczo, and R. J. Archuleta (2002), Efficient methods to simulate planar free surface in the 3d 4th -order staggered-grid finite-difference schemes, *Stud. Geophys. Geod.*, *46*, 355–381.

Lansing, D. L. (1966), The displacements in an elastic half-space due to a moving concentrated normal load, *Tech. Rep. R-238*, NASA.

Marcinkovich, C., and K. B. Olsen (2003), On the implementation of perfectly matched layers in a three-dimensional fourth-order velocity-stress finite difference scheme, *J. Geophys. Res.*, *108*(B5), 2276, doi:10.1029/2002JB002235.

Obrezanova, O., and J. R. Willis (2003), Stability of intersonic shear crack propagation, *J. Mech. Phys. Solids*, *51*(11), 1957–1970, doi:10.1016/j.jmps.2003.09.008.

Rice, J. R., C. G. Sammis, and R. Parsons (2005), Off-fault secondary failure induced by a dynamic slip-pulse, *Bull. Seismol. Soc. Am.*, *95*(1), 109–134, doi:10.1785/0120030166.

Robinson, D. P., C. Brough, and S. Das (2006), The Mw 7.8, 2001 Kunlunshan earthquake: Extreme rupture speed variability and effect of fault geometry, *J. Geophys. Res.*, *111*, B08303, doi:10.1029/2005JB004137.

Rosakis, A. J., O. Samudrala, and D. Coker (1999), Cracks faster than the shear wave speed, *Science*, *284*, 1337–1340.

Savage, J. C. (1971), Radiation from supersonic faulting, *Bull. Seismol. Soc. Am.*, *61*, 1009–1012.

Somerville, P. G., N. F. Smith, R. W. Graves, and N. A. Abrahamson (1997), Modification of empirical strong ground motion attenuation relations to include the amplitude and duration effects of rupture directivity, *Seismol. Res. Lett.*, *68*, 199–222.

Spudich, P., and E. Cranswick (1984), Direct observation of rupture propagation during the 1979 Imperial Valley earthquake using a short baseline accelerometer array, *Bull. Seismol. Soc. Am.*, *74*(6), 2083–2114.

Spudich, P., and M. Guatteri (2004), The effect of bandwidth limitations on the inference of earthquake slip-weakening distance from seismograms, *Bull. Seismol. Soc. Am.*, *94*(6), 2028–2036, doi:10.1785/0120030104.

Xia, K., A. J. Rosakis, and H. Kanamori (2004), Laboratory earthquakes: The sub-Rayleigh-to-supershear transition, *Science*, *303*(5665), 1859–1861, doi:10.1126/science.1094022.

H. S. Bhat, Department of Earth Sciences, University of Southern California, Zumberge Hall of Science, 264B, 3651 Trousdale Parkway, Los Angeles, CA 90089, USA. (hbhat@usc.edu)

E. M. Dunham, Department of Earth and Planetary Sciences and School of Engineering and Applied Sciences, Harvard University, 288 Pierce Hall, 29 Oxford Street, Cambridge, MA 02138, USA. (edunham@fas.harvard.edu)